

**Highly active ruthenium site stabilized by modulating electron-feeding for sustainable acidic oxygen evolution electrocatalysis**

Kexin Wang,<sup>a</sup> Yali Wang,<sup>b</sup> Bin Yang,<sup>a,c</sup> Zhongjian Li,<sup>a,c</sup> Xuetao Qin,<sup>e</sup> Qinghua Zhang,<sup>a</sup> Lecheng Lei,<sup>a,c</sup> Ming Qiu,<sup>\*b</sup> Gang Wu,<sup>\*d</sup> and Yang Hou<sup>\* a,c</sup>

<sup>a</sup> Key Laboratory of Biomass Chemical Engineering of Ministry of Education, College of Chemical and Biological Engineering, Zhejiang University, Hangzhou 310027, China

<sup>b</sup> Institute of Nanoscience and Nanotechnology, College of Physical Science and Technology, Central China Normal University, Wuhan 430079, China

<sup>c</sup> Institute of Zhejiang University-Quzhou, 78 Jiuhua Boulevard North, Quzhou 324000, China

<sup>d</sup> Department of Chemical and Biological Engineering, University at Buffalo, The State University of New York, Buffalo, NY, 14260 USA

<sup>e</sup> Beijing National Laboratory for Molecular Sciences, College of Chemistry and Molecular Engineering, College of Engineering and BIC-ESAT, Perking University, Beijing 100871, China

## Experimental section

### Synthesis of $\text{Mn}_{0.73}\text{Ru}_{0.27}\text{O}_{2-\delta}$ .

367 mg of  $\text{Mn}(\text{CH}_3\text{COO})_2$ , 79 mg of  $\text{KMnO}_4$ , and 414 mg of  $\text{RuCl}_3$  with millimolar ratios of 1.5 : 1 : 2 were dissolved in 25, 25, and 5.0 mL deionized (DI) water, respectively. Then, 25 mL of  $\text{KMnO}_4$  solution was poured into  $\text{Mn}(\text{CH}_3\text{COO})_2$  solution, and then  $\text{RuCl}_3$  solution was added into the mixed solution dropwise. After stirring for 1 hour at room temperature, the mixed solution was filtrated, and the obtained sample was further dried at 50 °C in a vacuum for overnight. Finally, the as-prepared precursor was annealed at 350 °C for 2 hours under Ar atmosphere to obtain  $\text{Mn}_{0.73}\text{Ru}_{0.27}\text{O}_{2-\delta}$ .

### Synthesis of $\text{Mn}_{0.73}\text{Ru}_{0.27}\text{O}_{2-\delta}\text{-T}$ .

367 mg of  $\text{Mn}(\text{CH}_3\text{COO})_2$ , 79 mg of  $\text{KMnO}_4$ , and 414 mg of  $\text{RuCl}_3$  with millimolar ratios of 1.5 : 1 : 2 were dissolved in 25, 25, and 5.0 mL deionized (DI) water, respectively. Then, 25 mL of  $\text{KMnO}_4$  solution was poured into  $\text{Mn}(\text{CH}_3\text{COO})_2$  solution and then  $\text{RuCl}_3$  solution was added into the mixed solution dropwise. After stirring for 1 hour at room temperature, the mixed solution was filtrated, and the obtained sample was further dried at 50 °C in a vacuum for overnight. Finally, the as-prepared precursor was annealed at 250, 450, and 550 °C for 2 hours under Ar atmosphere, and the obtained samples were denoted as  $\text{Mn}_{0.73}\text{Ru}_{0.27}\text{O}_{2-\delta}\text{-T}$  (T = 250, 450, and 550).

### Synthesis of $\text{Mn}_{0.75}\text{Ru}_{0.25}\text{O}_{2-\delta}$ .

367 mg of  $\text{Mn}(\text{CH}_3\text{COO})_2$ , 79 mg of  $\text{KMnO}_4$ , and 373 mg of  $\text{RuCl}_3$  with millimolar ratio of 1.5 : 1 : 1.8 were dissolved in 25, 25, and 5.0 mL DI water, respectively. Then, 25 mL of  $\text{KMnO}_4$  solution was poured into  $\text{Mn}(\text{CH}_3\text{COO})_2$  solution, and then  $\text{RuCl}_3$  solution was added into the mixed solution dropwise. After stirring for 1 hour at room temperature, the mixed solution was filtrated, and the obtained sample was further dried at 50 °C in a vacuum for overnight. Finally, the as-prepared precursor was annealed at 350 °C for 2 hours under an Ar atmosphere.

**Synthesis of  $\text{Mn}_{0.69}\text{Ru}_{0.31}\text{O}_{2-\delta}$ .**

367 mg of  $\text{Mn}(\text{CH}_3\text{COO})_2$ , 79 mg of  $\text{KMnO}_4$ , and 455 mg of  $\text{RuCl}_3$  with millimolar ratio of 1.5 : 1 : 2.2 were dissolved in 25, 25, and 5.0 mL DI water, respectively. Then, 25 mL of  $\text{KMnO}_4$  solution was poured into  $\text{Mn}(\text{CH}_3\text{COO})_2$  solution, and then  $\text{RuCl}_3$  solution was added into the mixed solution dropwise. After stirring for 1 hour at room temperature, the mixed solution was filtrated, and the obtained sample was further dried at 50 °C in a vacuum for overnight. Finally, the as-prepared precursor was annealed at 350 °C for 2 hours under Ar atmosphere.

**Synthesis of  $\text{Mn}_{0.73}\text{Ru}_{0.27}\text{O}_{2-\delta 1}$ .**

367 mg of  $\text{Mn}(\text{CH}_3\text{COO})_2$ , 79 mg of  $\text{KMnO}_4$ , and 414 mg of  $\text{RuCl}_3$  with millimolar ratios of 1.5 : 1 : 2 were dissolved in 25, 25, and 5.0 mL deionized (DI) water, respectively. Then, 25 mL of  $\text{KMnO}_4$  solution was poured into  $\text{Mn}(\text{CH}_3\text{COO})_2$  solution, and then  $\text{RuCl}_3$  solution was added into the mixed solution dropwise. After stirring for 1 hour at room temperature, the mixed solution was filtrated, and the obtained sample was further dried at 50 °C in a vacuum for overnight. Finally, the as-prepared precursor was annealed at 350 °C for 3 hours under Ar atmosphere to obtain  $\text{Mn}_{0.73}\text{Ru}_{0.27}\text{O}_{2-\delta 1}$ .

**Synthesis of  $\text{Mn}_{0.73}\text{Ru}_{0.27}\text{O}_2$ .**

367 mg of  $\text{Mn}(\text{CH}_3\text{COO})_2$ , 79 mg of  $\text{KMnO}_4$ , and 414 mg of  $\text{RuCl}_3$  with millimolar ratio of 1.5 : 1 : 2 were dissolved in 25, 25, and 5.0 mL deionized (DI) water, respectively. Then, 25 mL of  $\text{KMnO}_4$  solution was poured into  $\text{Mn}(\text{CH}_3\text{COO})_2$  solution and then  $\text{RuCl}_3$  solution was added into the mixed solution dropwise. After stirring for 1 hour at room temperature, the mixed solution was filtrated, and the obtained sample was further dried at 50 °C in a vacuum for overnight. Finally, the as-prepared precursor was annealed at 350 °C for 5 hours under  $\text{O}_2$  atmosphere.

**Synthesis of  $\text{MnO}_{2-\delta}$ .**

367 mg of  $\text{Mn}(\text{CH}_3\text{COO})_2$  and 79 mg of  $\text{KMnO}_4$  with millimolar ratio of 1.5 : 1 were dissolved in 25 and 25 mL DI water, respectively. Then, 25 mL of  $\text{KMnO}_4$  solution

was poured into  $\text{Mn}(\text{CH}_3\text{COO})_2$  solution. After stirring for 1 hour at room temperature, the mixed solution was filtrated, and the obtained sample was further dried at 50 °C in a vacuum for overnight. Finally, the as-prepared precursor was annealed at 350 °C for 2 hours under Ar atmosphere.

#### **Synthesis of $\text{MnIrO}_{2-\delta}$ .**

184 mg of  $\text{Mn}(\text{CH}_3\text{COO})_2$ , 40 mg of  $\text{KMnO}_4$ , and 353 mg of  $\text{IrCl}_3$  with millimolar ratio of 1.5 : 1 : 2 were dissolved in 25, 25, and 5.0 mL DI water, respectively. Then, 25 mL of  $\text{KMnO}_4$  solution was poured into  $\text{Mn}(\text{CH}_3\text{COO})_2$  solution, and then  $\text{IrCl}_3$  solution was added into the mixed solution dropwise. After stirring for 1 hour at room temperature, the mixed solution was filtrated, and the obtained sample was further dried at 50 °C in a vacuum for overnight. Finally, the as-prepared precursor was annealed at 350 °C for 2 hours under Ar atmosphere.

#### **Electrode preparation.**

10.0 mg of catalyst was added to 1.0 mL of ethanol containing 10  $\mu\text{L}$  Nafion aqueous solution (5 wt.%, Sigma-Aldrich), and dispersed by sonication for 30 min to generate a homogeneous ink. 2.0  $\mu\text{L}$  of the catalyst ink was drop-casted on the surface of a glassy carbon electrode with a loading amount of 0.28  $\text{mg cm}^{-2}$  and dried in air at room temperature.

#### **Electrochemical tests.**

Electrochemical OER measurement was employed at room temperature using an electrochemical analyzer (CHI 760 E) in a typical three-electrode configuration where the graphite rod, electrocatalyst, and the Ag/AgCl electrode worked as counter electrode, working electrode, and reference electrode, respectively. Before testing, the electrocatalyst was cycled in the potential ranges from 1.0 to 1.4 V vs. Ag/AgCl until a steady CV curve was obtained. Linear sweep voltammetry (LSV) was tested at a scan rate of 5  $\text{mV s}^{-1}$ . The frequency of EIS was arranged from 100 kHz to 0.01 Hz, and the EIS results were presented in the form of Nyquist plot and fitted using ZView software with a representative equivalent electrical circuit. The ECSA was measured

from the electrochemical double-layer capacitance ( $C_{dl}$ ) by analyzing CV curves at various scan rates of 10, 30, 50, 70, 90, and 110  $\text{mV s}^{-1}$ . 1,000 CV cycles and chronopotentiometry tests were carried out to estimate the durability of electrocatalysts. All the measured potentials in 0.5 M  $\text{H}_2\text{SO}_4$  electrolyte were converted to the reversible hydrogen electrode (RHE) via the Nernst equation ( $E_{\text{RHE}} = E_{\text{Ag/AgCl}} + 0.059 \times \text{pH} + 0.197$ ). All polarization curves were calibrated with  $iR$ -correction with the following equation:  $E_{\text{final}} = E_0 - (iR)$  V, in which  $E_0$  is the potential referenced to the polarization curve,  $i$  is the current at  $E_0$  and  $R$  results from the EIS figures. Faradaic efficiency was measured by using the gas chromatograph in an air-tight vessel. Typically, the pH-dependence measurement was carried out at 1.2 to 1.6 V vs. RHE in 0.1 M  $\text{H}_2\text{SO}_4$  (pH = 0.7) and 0.05 M  $\text{H}_2\text{SO}_4$  (pH = 1.0), and the EOR was tested from 1.2 to 1.6 V vs. RHE with 5  $\text{mV s}^{-1}$  under 0.5 M  $\text{H}_2\text{SO}_4$  and 1.0 M ethanol mixed electrolyte.

### **Characterizations.**

X-ray diffraction (XRD, PANalytical) was tested to characterize the crystal structure of as-prepared samples. Field-emission scanning electron microscope (FESEM, Hitachi SU-8010), high-resolution transmission electron microscope (HRTEM Tecnai G2 F20S-TWIN) and High-angle annular dark-field scanning transmission electron microscope (HAADF-STEM) were applied to observe the microscopic morphology of as-prepared samples. Energy-dispersive X-ray spectroscopy (EDX, Oxford X-max80) equipped with HR-TEM was conducted to verify the actual distribution of elements in samples. X-ray photoelectron spectroscopy (XPS, Thermo Fisher Scientific, Escalab 250Xi) with Al  $K\alpha$  radiation was utilized to analyze the valence of major elements in samples. The 1W1B station in Beijing Synchrotron Radiation Facility (BSRF) and BL14W1 station in Shanghai Synchrotron Radiation Facility (SSRF) were employed for collecting X-ray absorption fine structure (XAFS) data of Ru and Mn elements. Soft X-ray magnetic circular dichroism end station (XMCD) of the National Synchrotron Radiation Laboratory (NSRL) in University of Science and Technology

of China (USTC) was applied to measure O K-edge and Mn L-edge. XAS measurements were conducted on the 1W1B station in Beijing Synchrotron Radiation Facility (BSRF) and Shanghai Synchrotron Radiation Facility. Inductively coupled plasma analysis (ICP-OES/MS 730-ES) was used to measure the contents of Mn and Ru species in samples. AUTOSORB-IQ-MP was selected to measure the Brunner-Emmet-Teller (BET) surface area and pore-size distributions at 77 K.

### Computational methods

The spin-polarized generalized gradient approximation (SGGA) within Perdew-Burke-Ernzerhof (PBE) form was set up as an exchange-correlation function. A 3 x 3 x 1 Monkhorst-Pack k-points grid was used for k-points sampling, and a 900 eV plane-wave expansion was set up for energy cut-offs. These parameters were carefully tested. The Ru-4d<sup>7</sup>5s<sup>1</sup>, Mn-3d<sup>5</sup>4s<sup>2</sup>, O-2s<sup>2</sup>2p<sup>4</sup>, C-2s<sup>2</sup>2p<sup>2</sup>, and H-1s<sup>1</sup> were setup for valence states. A vacuum slab of about 15 Å was maintained in the super-cell configuration that was large enough for the calculations. The SCF tolerance for geometrical optimization and phonon calculations was less than 1e<sup>-6</sup> eV·atom<sup>-1</sup>.

The reaction pathways for O<sub>2</sub> evolution in the OER process are simulated as the following:



In these equations, the \* denotes the catalytic active site on surface; the OH\*, O\*, H<sub>2</sub>O\*, and OOH\* denote the reaction intermediates with adsorbed groups of OH, O, H<sub>2</sub>O, and OOH, respectively.

For the free energies calculations, the Zero-point energy (ZPE) and entropy corrections are considered in the absorption energies parts. The equation is as follows:

$$\Delta G_{ads} = \Delta E_{ads} + \Delta ZPE - T\Delta S \quad \text{S5}$$

For each elementary reaction step, the reaction free energy is calculated by:

$$\Delta G = \Delta E + \Delta ZPE - T\Delta S + \Delta G_U + \Delta G_{pH}$$

S6

The reaction energy difference between reactant and product is denoted as  $\Delta E$ ; the free energy of product  $\Delta G_U$  is dependent on the electrode potential  $V$  and electron charge  $e$ .

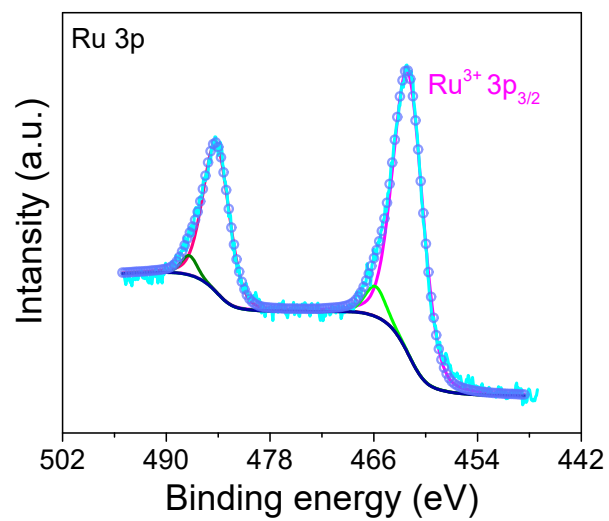


**Fig. S1** High-resolution XPS spectrum of Ru 3p for Mn<sub>0.73</sub>Ru<sub>0.27</sub>O<sub>2- $\delta$</sub>  (pre).

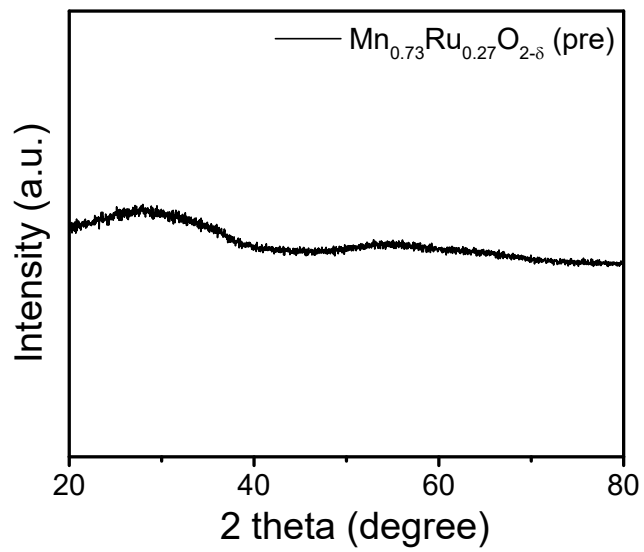


**Fig. S2** XRD pattern of precursor  $\text{Mn}_{0.73}\text{Ru}_{0.27}\text{O}_{2-\delta}$  (pre).

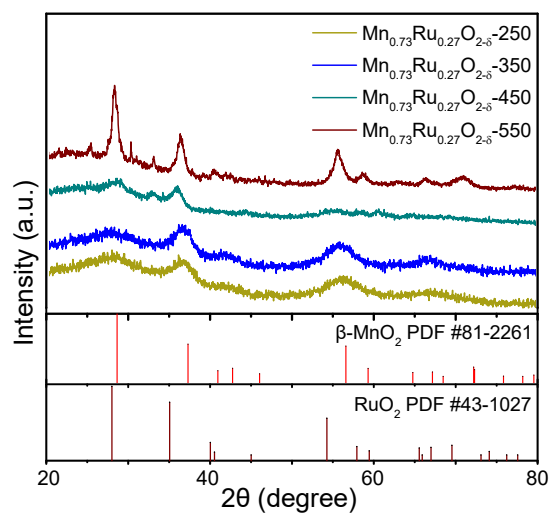


**Fig. S3** XRD patterns of  $\text{Mn}_{0.73}\text{Ru}_{0.27}\text{O}_{2-\delta}$ -250,  $\text{Mn}_{0.73}\text{Ru}_{0.27}\text{O}_{2-\delta}$ -350,  $\text{Mn}_{0.73}\text{Ru}_{0.27}\text{O}_{2-\delta}$ -450, and  $\text{Mn}_{0.73}\text{Ru}_{0.27}\text{O}_{2-\delta}$ -550.

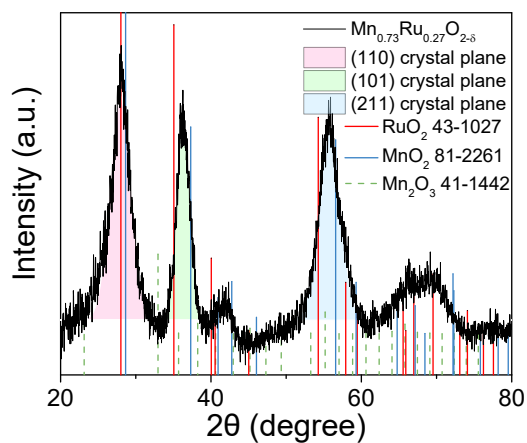


**Fig. S4** XRD refinement pattern for the  $\text{Mn}_{0.73}\text{Ru}_{0.27}\text{O}_{2-\delta}$ .

We calculated the average diameter of  $\text{Mn}_{0.73}\text{Ru}_{0.27}\text{O}_{2-\delta}$  nanoparticles, according to the Debye-Scherrer's equation.

$$D = \frac{K\lambda}{\beta \cos \theta}$$

Where, D represents the average dimension of crystallites,  $K = 0.94$ ,  $\lambda$  is wavelength of the  $\text{CuK}\alpha$ .

The average diameter of  $\text{Mn}_{0.73}\text{Ru}_{0.27}\text{O}_{2-\delta}$  nanoparticles was calculated to about 3 nm (Table S2), which confirmed that the  $\text{Mn}_{0.73}\text{Ru}_{0.23}\text{O}_{2-d}$  sample in this work was nanoscale particles.

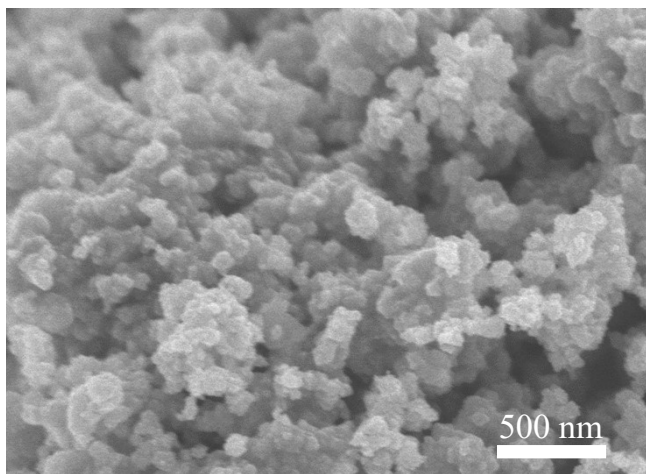


**Fig. S5** FESEM image of the  $\text{Mn}_{0.73}\text{Ru}_{0.27}\text{O}_{2-\delta}$ .

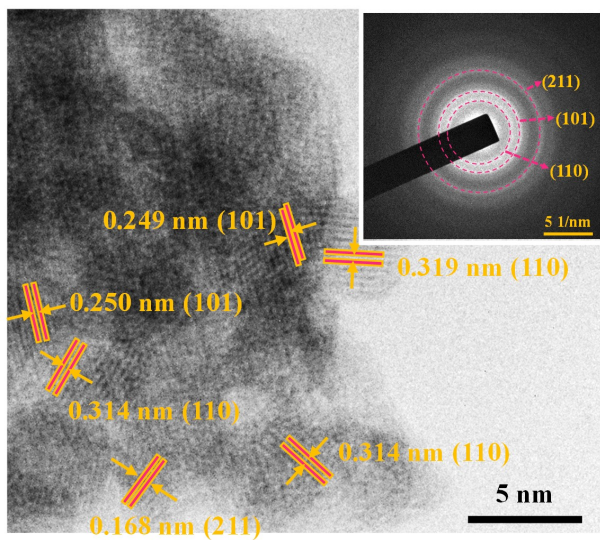


**Fig. S6** HRTEM image of Mn<sub>0.73</sub>Ru<sub>0.27</sub>O<sub>2-δ</sub>, inset: corresponding SAED pattern.

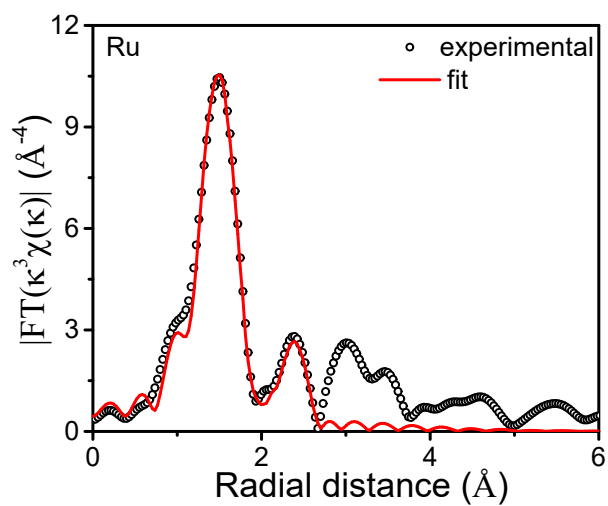


**Fig. S7** Fitting results of R-space EXAFS at the Ru K-edge for the  $\text{Mn}_{0.73}\text{Ru}_{0.27}\text{O}_{2-\delta}$ .

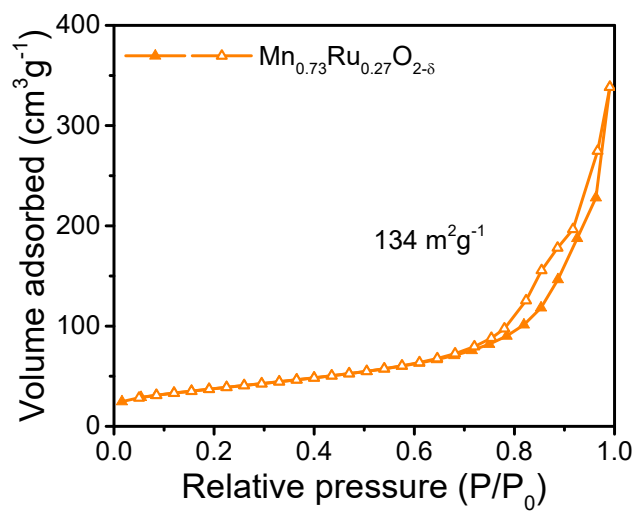


**Fig. S8** N<sub>2</sub> adsorption isotherm curve of the Mn<sub>0.73</sub>Ru<sub>0.27</sub>O<sub>2-δ</sub>.

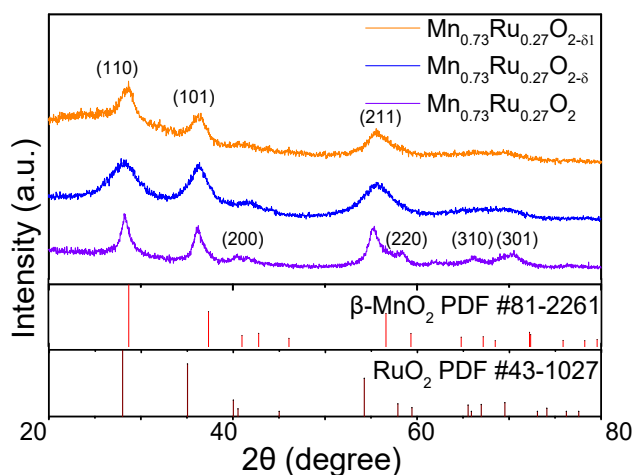


**Fig. S9** XRD patterns of  $\text{Mn}_{0.73}\text{Ru}_{0.27}\text{O}_2$ ,  $\text{Mn}_{0.73}\text{Ru}_{0.27}\text{O}_{2-\delta}$  and  $\text{Mn}_{0.73}\text{Ru}_{0.27}\text{O}_{2-\delta 1}$ .

In the XRD pattern of  $\text{Mn}_{0.73}\text{Ru}_{0.27}\text{O}_2$ , the remaining minor peaks of  $40.3^\circ$ ,  $58.5^\circ$ ,  $66.2^\circ$  and  $70.5^\circ$  all located between  $\text{RuO}_2$  and  $\beta\text{-MnO}_2$  could be assigned to the (200), (220), (310), and (301) crystal planes of rutile solid-solution oxides following Vegard's law. It is clearly seen that besides the structures of rutile solid-solution oxides, no any other phases were observed for  $\text{Mn}_{0.73}\text{Ru}_{0.27}\text{O}_2$ , indicating that the changes in heating conditions did not cause the formation of new species.

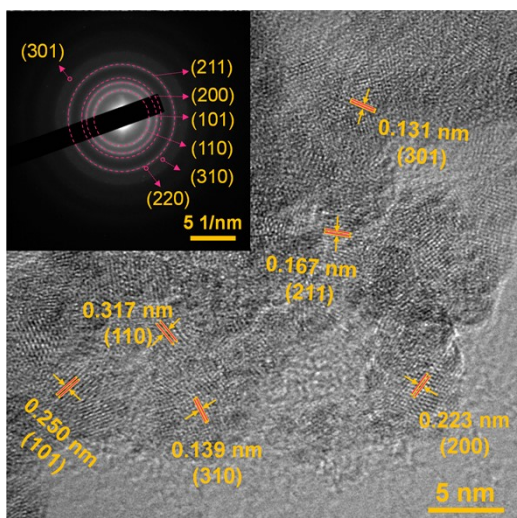


**Fig. S10** HRTEM image of Mn<sub>0.73</sub>Ru<sub>0.27</sub>O<sub>2</sub>.

The particle size of Mn<sub>0.73</sub>Ru<sub>0.27</sub>O<sub>2</sub> still remained about 3 nm, and no any lattice distances attributing to metal Ru and Mn species were found, which excluded the formation of exsolved metal nanoparticles.

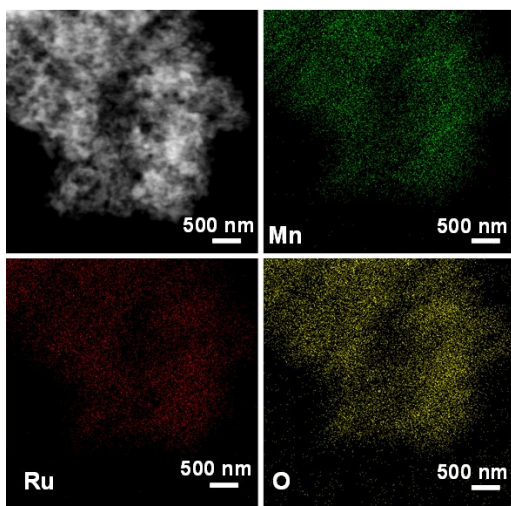


**Fig. S11** EDX elemental mapping images of  $\text{Mn}_{0.73}\text{Ru}_{0.27}\text{O}_2$ , including the Mn, Ru, and O elements.

The exclusion of the formation of exsolved metal nanoparticles was further supported by EDX elemental mapping images, in which the Ru, Mn, and O elements were homogeneously distributed on the surface of  $\text{Mn}_{0.73}\text{Ru}_{0.27}\text{O}_2$ .

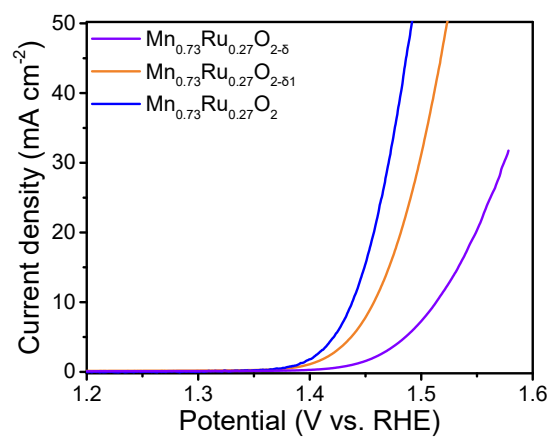


**Fig. S12** Polarization curves of Mn<sub>0.73</sub>Ru<sub>0.27</sub>O<sub>2-δ</sub>, Mn<sub>0.73</sub>Ru<sub>0.27</sub>O<sub>2-δ1</sub> and Mn<sub>0.73</sub>Ru<sub>0.27</sub>O<sub>2</sub>.

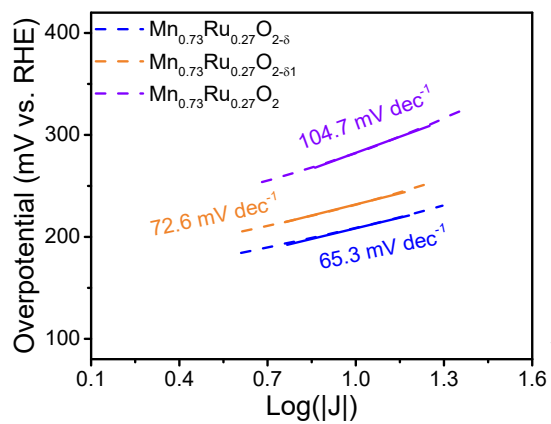


**Fig. S13** Tafel slopes of  $\text{Mn}_{0.73}\text{Ru}_{0.27}\text{O}_{2-\delta}$ ,  $\text{Mn}_{0.73}\text{Ru}_{0.27}\text{O}_{2-\delta 1}$  and  $\text{Mn}_{0.73}\text{Ru}_{0.27}\text{O}_2$ .

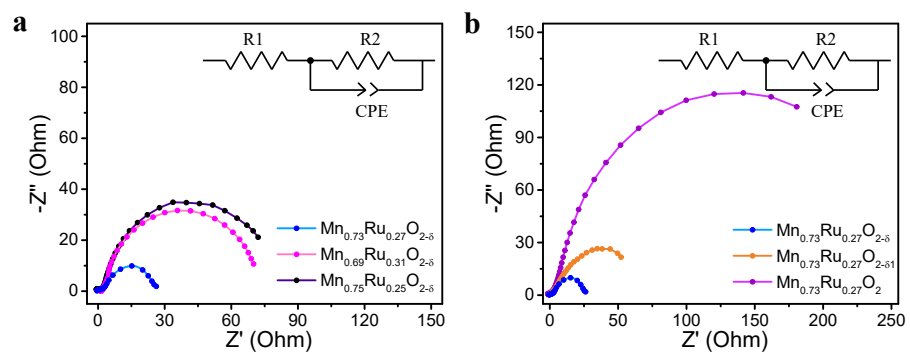


**Fig. S14** Nyquist plots of (a)  $\text{Mn}_{0.73}\text{Ru}_{0.27}\text{O}_{2-\delta}$ ,  $\text{Mn}_{0.69}\text{Ru}_{0.31}\text{O}_{2-\delta}$ ,  $\text{Mn}_{0.75}\text{Ru}_{0.25}\text{O}_{2-\delta}$ , (b)  $\text{Mn}_{0.73}\text{Ru}_{0.27}\text{O}_{2-\delta1}$ , and  $\text{Mn}_{0.73}\text{Ru}_{0.27}\text{O}_2$ .

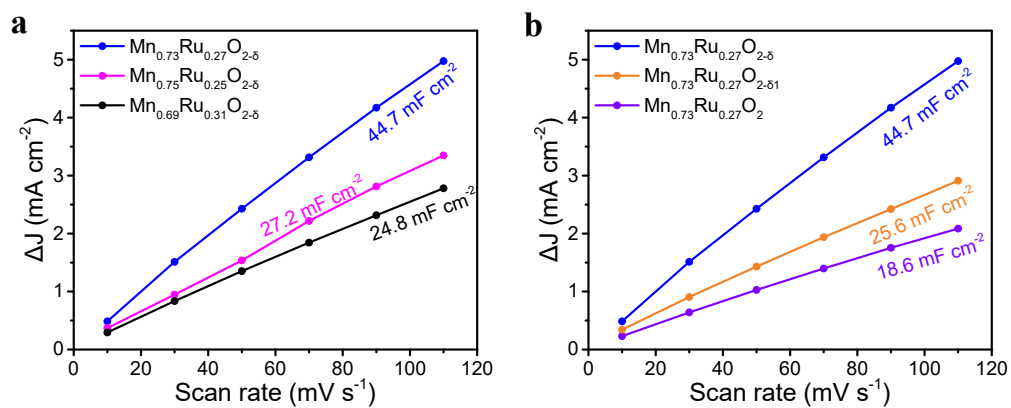


**Fig. S15** ECSA curves for (a) Mn<sub>0.73</sub>Ru<sub>0.27</sub>O<sub>2-δ</sub>, Mn<sub>0.69</sub>Ru<sub>0.31</sub>O<sub>2-δ</sub>, Mn<sub>0.75</sub>Ru<sub>0.25</sub>O<sub>2-δ</sub>, (b) Mn<sub>0.73</sub>Ru<sub>0.27</sub>O<sub>2-δ₁</sub>, and Mn<sub>0.73</sub>Ru<sub>0.27</sub>O<sub>2</sub>.

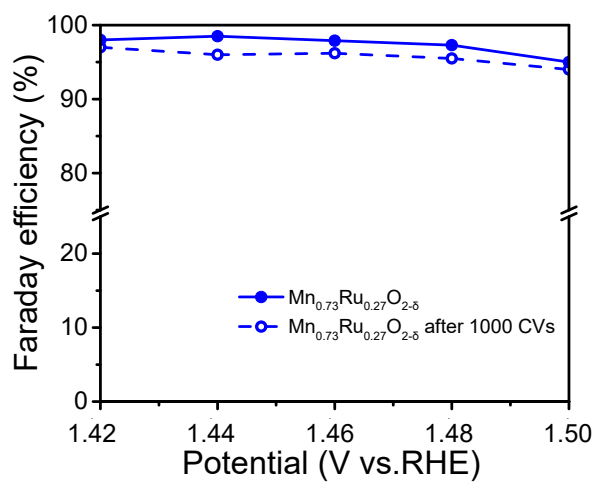


**Fig. S16** Faraday efficiencies for Mn<sub>0.73</sub>Ru<sub>0.27</sub>O<sub>2-δ</sub> and Mn<sub>0.73</sub>Ru<sub>0.27</sub>O<sub>2-δ</sub> after 1000 CVs.

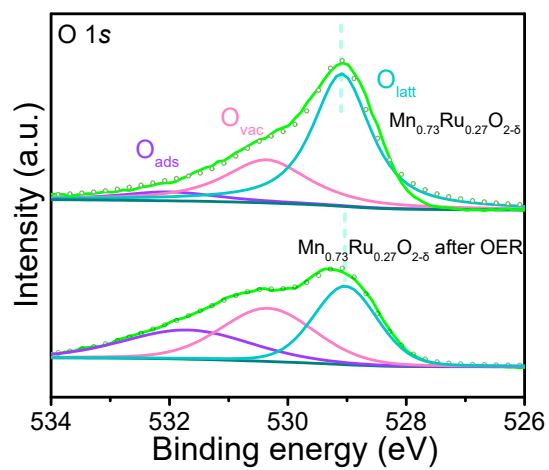


**Fig. S17** High-resolution XPS spectra of O 1s for  $\text{Mn}_{0.73}\text{Ru}_{0.27}\text{O}_{2-\delta}$  and  $\text{Mn}_{0.73}\text{Ru}_{0.27}\text{O}_{2-\delta}$  after OER.

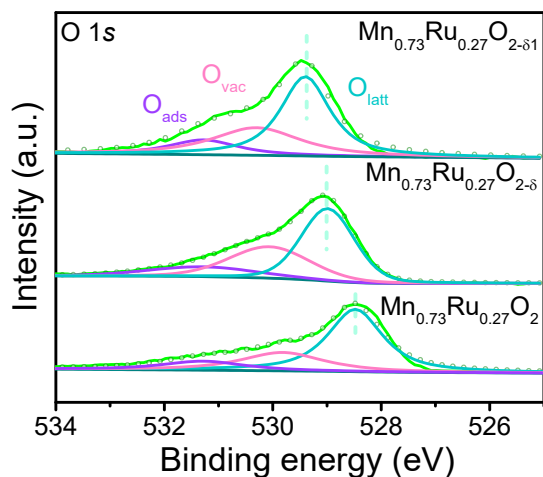


**Fig. S18** High-resolution XPS of O 1s spectra for  $\text{Mn}_{0.73}\text{Ru}_{0.27}\text{O}_{2-\delta 1}$ ,  $\text{Mn}_{0.73}\text{Ru}_{0.27}\text{O}_{2-\delta}$  and  $\text{Mn}_{0.73}\text{Ru}_{0.27}\text{O}_2$ .

As the formation of oxygen vacancies is endothermic, a prolonged dwell time favors a high concentration of oxygen vacancies<sup>1</sup>.

In view of the considerable influence of oxygen vacancies towards OER performance, the ratio of  $O_{\text{vac}}/O_{\text{latt}}$  (peak area from Fig. S17) was calculated as a yardstick to estimate the relative amount of surface oxygen vacancies<sup>2</sup>. As shown in Table S7, the  $\text{Mn}_{0.73}\text{Ru}_{0.27}\text{O}_{2-\delta 1}$  with the highest  $O_{\text{vac}}/O_{\text{latt}}$  ratio possessed the most oxygen vacancy amount, followed by  $\text{Mn}_{0.73}\text{Ru}_{0.27}\text{O}_{2-\delta}$  and  $\text{Mn}_{0.73}\text{Ru}_{0.27}\text{O}_2$ . Comparing the corresponding OER performances with these catalysts (Fig. S12), the  $\text{Mn}_{0.73}\text{Ru}_{0.27}\text{O}_{2-\delta}$  catalyst with appropriate amount of oxygen vacancy displayed the best OER catalytic activity, which demonstrated that the oxygen vacancy formed in the  $\text{Mn}_{0.73}\text{Ru}_{0.27}\text{O}_{2-\delta}$  played a certain role in enhancing OER activity.

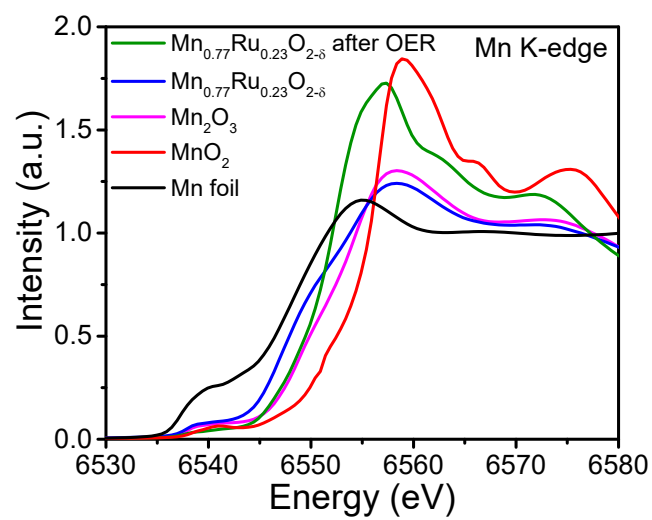


**Fig. S19** XANES spectra at the Mn K-edge for  $\text{Mn}_{0.73}\text{Ru}_{0.27}\text{O}_{2-\delta}$  after OER,  $\text{Mn}_{0.73}\text{Ru}_{0.27}\text{O}_{2-\delta}$ ,  $\text{MnO}_2$ ,  $\text{Mn}_2\text{O}_3$ , and Mn foil.

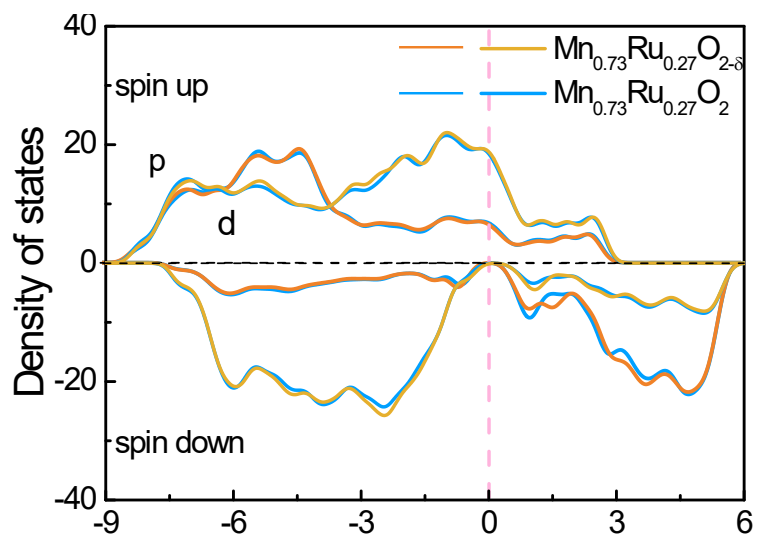


**Fig. S20** PDOS of p and d orbitals calculations for  $\text{Mn}_{0.73}\text{Ru}_{0.27}\text{O}_{2-\delta}$  and  $\text{Mn}_{0.73}\text{Ru}_{0.27}\text{O}_2$ .

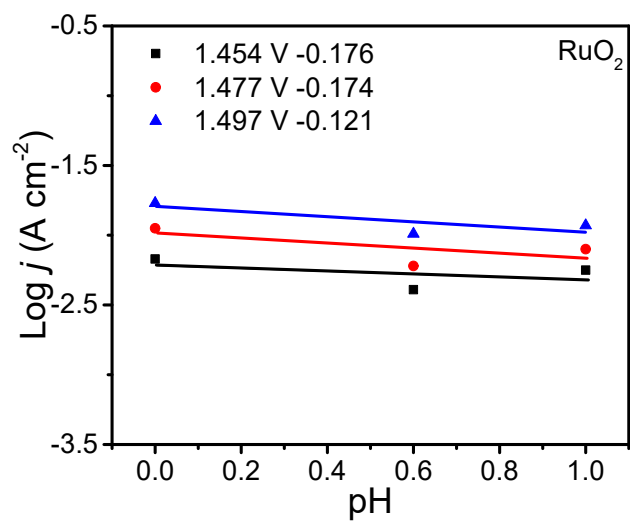


**Fig. S21** pH-independence of the OER activities for RuO<sub>2</sub>.

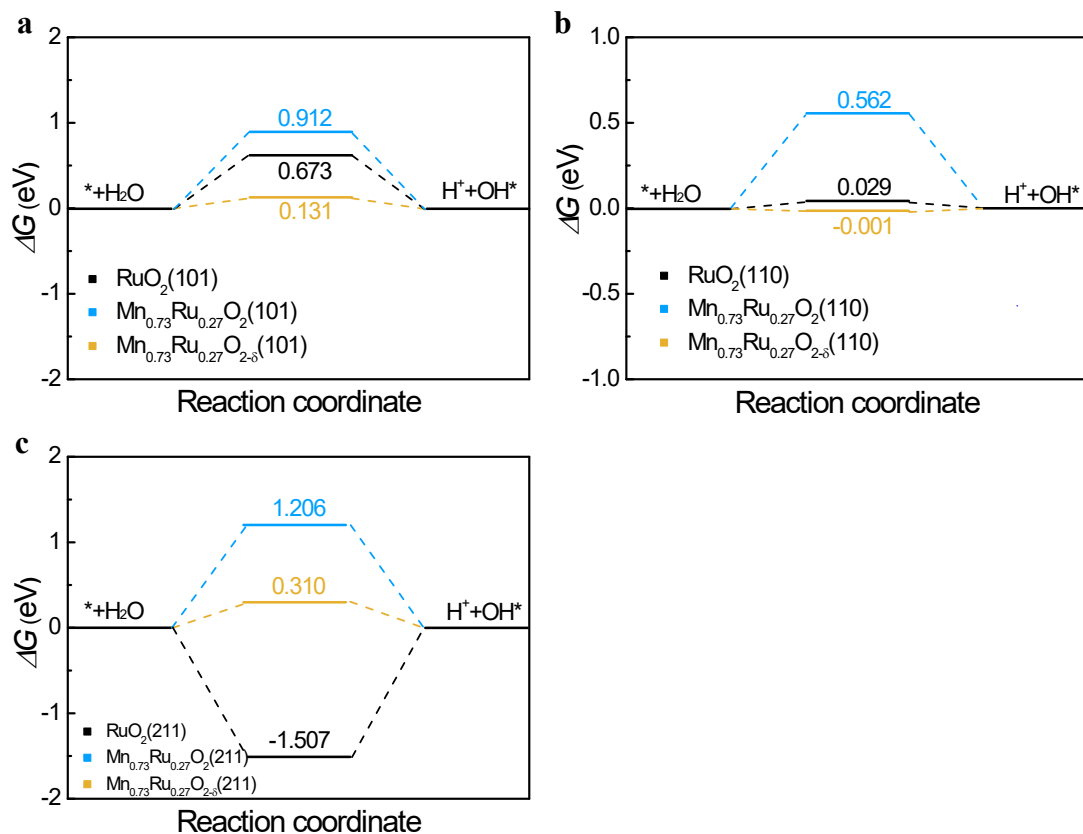


**Fig. 22** The Gibbs free energy diagrams of water dissociation in acid for  $\text{Mn}_{0.73}\text{Ru}_{0.27}\text{O}_{2-\delta}$ ,  $\text{Mn}_{0.73}\text{Ru}_{0.27}\text{O}_2$ , and  $\text{RuO}_2$  at the lattice planes of (a) (101), (b) (110), and (c) (211).

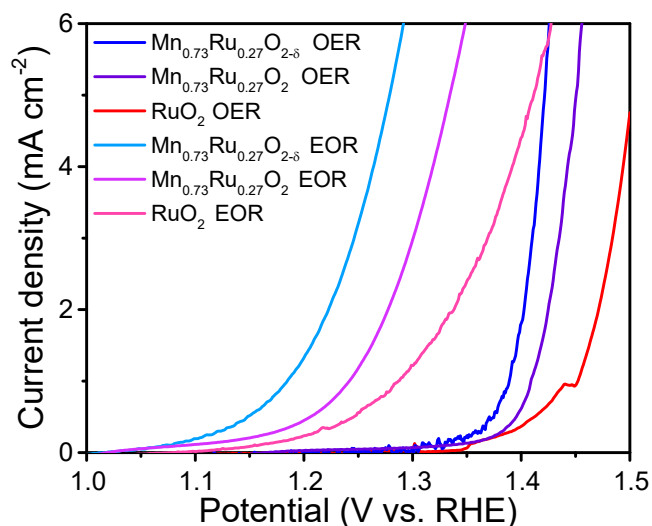


**Fig. S23** EOR and OER polarization curves for  $\text{Mn}_{0.73}\text{Ru}_{0.27}\text{O}_{2-\delta}$ ,  $\text{Mn}_{0.73}\text{Ru}_{0.27}\text{O}_2$ , and  $\text{RuO}_2$ .

Considering the  $\text{OH}^*$  is first and essential intermediate during the OER mechanism, the experiment of EOR was conducted to represent the  $\text{OH}^*$  adsorption strength of catalysts. Due to the fast reaction kinetics of EOR with  $\text{OH}^*$  intermediate, the distinct fingerprint in current-potential influenced by ethanol oxidation could be used to uncover the  $\text{OH}^*$  bonding energy that governs kinetics of OER.

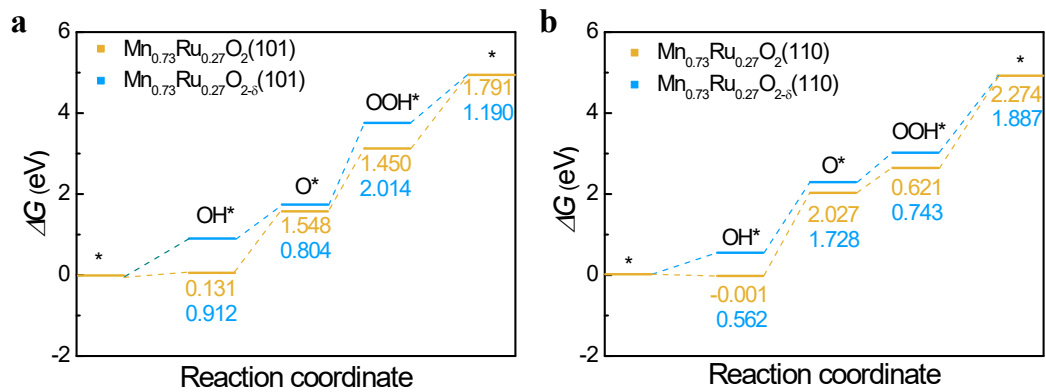


**Fig. S24** The Gibbs free energy diagrams of  $\text{Mn}_{0.73}\text{Ru}_{0.27}\text{O}_{2-\delta}$  and  $\text{Mn}_{0.73}\text{Ru}_{0.27}\text{O}_2$  at the lattice planes of (a) (101) and (b) (110) for OER.

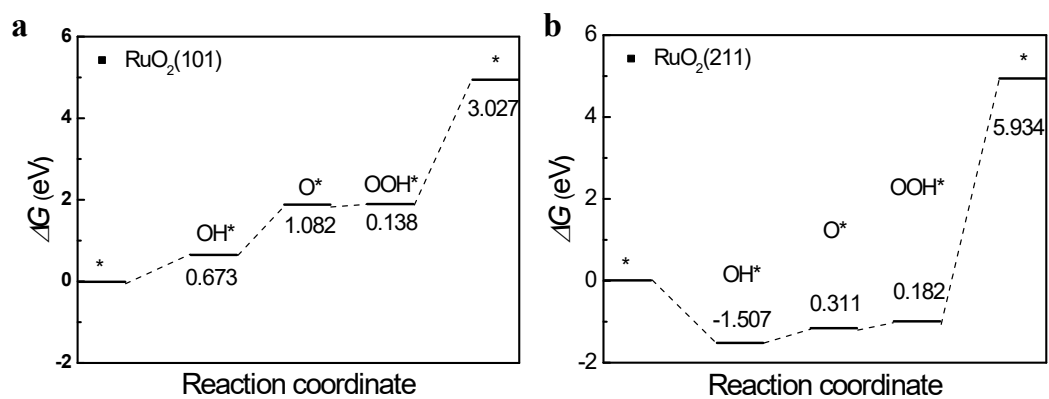


**Fig. S25** The Gibbs free energy diagrams of  $\text{RuO}_2$  at lattice planes of (a) (101) and (b) (211) for OER.

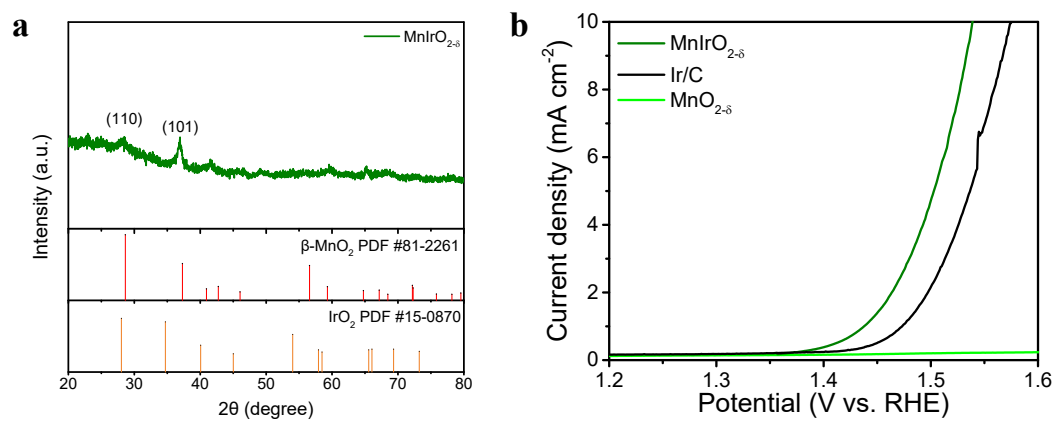


**Fig. S26** (a) XRD pattern of MnIrO<sub>2-δ</sub>. (b) Polarization curves for MnIrO<sub>2-δ</sub>, Ir/C, and MnO<sub>2-δ</sub>.

**Table S1.** The molar percent of Mn and Ru species for  $\text{Mn}_{1-x}\text{Ru}_x\text{O}_{2-\delta}$  measured by ICP-OES analysis.

Molar ratio of raw material ( $\text{Mn}(\text{CH}_3\text{COO})_2$ : $\text{KMnO}_4$ : $\text{RuCl}_3$ )	Sample amount (mg)	Concentration of Ru ion ( $\text{mg L}^{-1}$ )	Concentration of Mn ion ( $\text{mg L}^{-1}$ )	Ru molar ratio among metals (x)
1.5 : 1: 1.8	38.8	5.92	9.78	0.25
1.5 : 1: 2	42.1	6.53	9.51	0.27
1.5 : 1: 2.2	33.3	6.22	7.99	0.31

**Table S2.** Particle size calculation based on Debye-Scherrer's equation.

<b>Material</b>	<b>2<math>\theta</math></b>	<b>FWHM</b>	<b>Crystallite size (nm)</b>
$\text{Mn}_{0.75}\text{Ru}_{0.25}\text{O}_{2-\delta}$	28.66	7.89	1.09
	36.05	3.69	2.37
	55.42	4.76	1.98
$\text{Mn}_{0.73}\text{Ru}_{0.23}\text{O}_{2-\delta}$	28.08	3.63	2.36
	36.3	2.4	3.65
	55.72	4.33	2.17
$\text{Mn}_{0.69}\text{Ru}_{0.31}\text{O}_{2-\delta}$	27.98	3.47	2.47
	36.31	2.14	4.09
	55.77	3.62	2.60

**Table S3.** Structural parameters of  $\text{Mn}_{0.73}\text{Ru}_{0.27}\text{O}_{2-\delta}$  extracted from the EXAFS fitting ( $S_0^2 = 0.85$ ).

Sample	Scattering pair	CN	R(Å)	$\sigma^2(10^{-3}\text{Å}^2)$	$\Delta E_0(\text{eV})$	R
$\text{Mn}_{0.73}\text{Ru}_{0.27}\text{O}_{2-\delta}$	Ru-O	5.6(2)	1.95(2)	3.5(1)	-6.6(3)	0.02
	Ru-Ru	1.1(1)	2.82(2)	6.5(2)	-6.6(3)	
	Mn-O	3.8(3)	1.93(2)	3.8(3)	-4.1(3)	0.02
	Mn-Mn	2.1(2)	2.85(2)	5.7(5)	-4.1(4)	

$S_0^2$  is the amplitude reduction factor; CN is the coordination number; R is the interatomic distance (the bond length between central atoms and surrounding coordination atoms);  $\sigma^2$  is Debye-Waller factor (a measure of thermal and static disorder in absorber-scatter distances);  $\Delta E_0$  is edge-energy shift (the difference between the zero kinetic energy value of the sample and that of the theoretical model). R factor is used to value the goodness of the fitting.

**Table S4.** Comparison of OER performances in acid for  $\text{Mn}_{0.73}\text{Ru}_{0.27}\text{O}_{2-\delta}$  with those representative noble metal-based OER electrocatalysts.

Catalyst	Electrolyte	Potential at the	Tafel	Stability	Ref.
		10 mA cm <sup>-2</sup> (vs. RHE)	slope (mV dec <sup>-1</sup> )		
<b><math>\text{Mn}_{0.73}\text{Ru}_{0.27}\text{O}_{2-\delta}</math></b>	<b>0.5 M <math>\text{H}_2\text{SO}_4</math></b>	<b>208 mV</b>	<b>65.3</b>	<b>10 h @ 10 mA cm<sup>-2</sup></b>	<b>This work</b>
np-Ir <sub>70</sub> Ni <sub>15</sub> Co <sub>15</sub>	0.5 M $\text{H}_2\text{SO}_4$	220 mV	44.1	24 h @ 1.45 V	3
Amorphous Ir NSs	0.5 M $\text{H}_2\text{SO}_4$	255 mV	40	24 h @ 1.45 V	4
IrO <sub>2</sub> -RuO <sub>2</sub> @Ru	0.5 M $\text{H}_2\text{SO}_4$	281 mV	53.1	20 h @ 1.5 V	5
Ru@IrOx	0.05 M $\text{H}_2\text{SO}_4$	282 mV	69.1	24 h @ 1.55 V	6
Ru-N-C	0.05 M $\text{H}_2\text{SO}_4$	267 mV	52.6	30 h @ 1.5 V	7
HNC-Co	0.5 M $\text{H}_2\text{SO}_4$	265 mV	85	20 h @ 1.7 V	8
Ir-NiCo <sub>2</sub> O <sub>4</sub>	0.5 M $\text{H}_2\text{SO}_4$	240 mV	60	70 h @ 10 mA cm <sup>-2</sup>	9
Rh <sub>22</sub> Ir <sub>78</sub>	0.5 M $\text{H}_2\text{SO}_4$	292 mV	101	10 h @ 1.5 V	10

RuO <sub>2</sub> nanosheets	0.5 M H <sub>2</sub> SO <sub>4</sub>	255 mV	38	3 h @ 10 mA cm <sup>-2</sup>	11
RuIrO <sub>x</sub>	0.5 M H <sub>2</sub> SO <sub>4</sub>	220 mV	42	24 h @ 1.45 V	12
IrCuNi	0.5 M H <sub>2</sub> SO <sub>4</sub>	273 mV	41	10 h @ 1.5 V	13
RuCu nanoalloy	0.5 M H <sub>2</sub> SO <sub>4</sub>	270 mV	75.8	20 h @ 10 mA cm <sup>-2</sup>	14
h-PNRO/C	0.1 M HClO <sub>4</sub>	239 mV	52	10 h @ 10 mA cm <sup>-2</sup>	15
Y <sub>1.85</sub> Zn <sub>0.15</sub> Ru <sub>2</sub> O <sub>7-δ</sub>	0.5 M H <sub>2</sub> SO <sub>4</sub>	290 mV	36.9	10 h @ 1.5 V	16
Mn44 (Mn promoted TiO <sub>2</sub> -RuO <sub>2</sub> )	0.1 M H <sub>2</sub> SO <sub>4</sub>	386 mV	50	6 h @ 1 mA cm <sup>-2</sup>	17
Ru(0.1)-MnO <sub>2</sub>	0.5 M H <sub>2</sub> SO <sub>4</sub>	279 mV	NA	NA	18
IrRuMn/C	0.1 M HClO <sub>4</sub>	260 mV	45.6	8 h @ 10 mA cm <sup>-2</sup>	19

---

**Table S5.** Summary of impedance fitting data for  $\text{Mn}_{0.73}\text{Ru}_{0.27}\text{O}_{2-\delta}$ ,  $\text{Mn}_{0.73}\text{Ru}_{0.27}\text{O}_{2-\delta 1}$ ,  $\text{Mn}_{0.69}\text{Ru}_{0.31}\text{O}_{2-\delta}$ ,  $\text{Mn}_{0.75}\text{Ru}_{0.25}\text{O}_{2-\delta}$ , and  $\text{Mn}_{0.73}\text{Ru}_{0.27}\text{O}_2$ .

	$\text{Mn}_{0.73}\text{Ru}_{0.27}\text{O}_{2-\delta}$	$\text{Mn}_{0.73}\text{Ru}_{0.27}\text{O}_{2-\delta 1}$	$\text{Mn}_{0.69}\text{Ru}_{0.31}\text{O}_{2-\delta}$	$\text{Mn}_{0.75}\text{Ru}_{0.25}\text{O}_{2-\delta}$	$\text{Mn}_{0.73}\text{Ru}_{0.27}\text{O}_2$
R1 ( $\Omega$ )	14.07	14.12	14.36	75.62	15.39
R2 ( $\Omega$ )	22.4	63.26	70.92	75.62	266.8
CPE <sub>p</sub> (mF)	0.89	0.91	0.92	0.95	0.91

**Table S6.** ICP-MS results of dissolved Mn and Ru species for  $\text{Mn}_{0.73}\text{Ru}_{0.27}\text{O}_{2-\delta}$ ,  $\text{RuO}_2$ , and  $\text{RuO}_2$ -1 after OER test.

Sample	Sample amount	Concentrations of Ru ion ( $\mu\text{g mL}^{-1}$ ) / Mn ion ( $\mu\text{g mL}^{-1}$ )	Loss mass percent of Ru/Mn
$\text{Mn}_{0.73}\text{Ru}_{0.27}\text{O}_{2-\delta}$	20 $\mu\text{g}$ , 5 $\mu\text{mol}$ Ru	0.012/0.049	0.78%/3.18%
$\text{RuO}_2$	20 $\mu\text{g}$	0.076/0	2.95%/0
$\text{RuO}_2$ -1	5 $\mu\text{mol}$ Ru	0.003/0	2.41%/0

The  $\text{RuO}_2$ -1 is defined as commercial  $\text{RuO}_2$  with the same mol of Ru (5  $\mu\text{mol}$  Ru).

With the same mol Ru (5  $\mu\text{mol}$  Ru), the leaked amount of Ru in the  $\text{Mn}_{0.73}\text{Ru}_{0.27}\text{O}_{2-\delta}$  catalyst (0.78 %) was much lower than that of in the  $\text{RuO}_2$ -1 (2.41%). Meanwhile, with the same loading amount (20  $\mu\text{g}$ ), the leaked amount of Ru in the  $\text{Mn}_{0.73}\text{Ru}_{0.27}\text{O}_{2-\delta}$  catalyst (0.78 %) was also much lower than that of in the  $\text{RuO}_2$  (2.95%) mentioned in the manuscript. That is to say, under the same conditions of stability test, the difference in stability could be ascribed to the difference in the intrinsic property of catalyst, which is well supported by previous report<sup>20</sup>.

**Table S7.** The relative amounts of surface oxygen vacancies in  $\text{Mn}_{0.73}\text{Ru}_{0.27}\text{O}_{2-\delta_1}$ ,  $\text{Mn}_{0.73}\text{Ru}_{0.27}\text{O}_{2-\delta}$ , and  $\text{Mn}_{0.73}\text{Ru}_{0.27}\text{O}_2$  by analyzing the ratio  $\text{O}_{\text{vac}}/\text{O}_{\text{latt}}$  in high-resolution O 1s XPS spectral fitting.

	$\text{Mn}_{0.73}\text{Ru}_{0.27}\text{O}_{2-\delta_1}$	$\text{Mn}_{0.73}\text{Ru}_{0.27}\text{O}_{2-\delta}$	$\text{Mn}_{0.73}\text{Ru}_{0.27}\text{O}_2$
The ratio of $\text{O}_{\text{vac}}/\text{O}_{\text{latt}}$	0.61	0.47	0.42
Error (standard deviation)	0.0089	0.0029	0.0023

## References

1. C. Sun, Y. Wang, J. Zou, and S. C. Smith, *Phys. Chem. Chem. Phys.*, 2011, **13**, 11325.
2. Z. Xiao, Y. C. Huang, C. L. Dong, C. Xie, Z. Liu, S. Du, W. Chen, D. Yan, L. Tao, Z. Shu, G. Zhang, H. Duan, Y. Wang, Y. Zou, R. Chen and S. Wang, *J. Am. Chem. Soc.*, 2020, **142**, 12087-12095.
3. M. L. Yang Zhaoa, Shufen Chuc, Ming Penga, Boyang Liud, Qiuli Wua, Pan Liuc, and Y. T. Frank M.F. de Groote, *Nano Energy*, 2019, **59**, 8.
4. G. Wu, X. Zheng, P. Cui, H. Jiang, X. Wang, Y. Qu, W. Chen, Y. Lin, H. Li, X. Han, Y. Hu, P. Liu, Q. Zhang, J. Ge, Y. Yao, R. Sun, Y. Wu, L. Gu, X. Hong and Y. Li, *Nat Commun*, 2019, **10**, 4855.
5. G. Li, S. Li, J. Ge, C. Liu and W. Xing, *J. Mater. Chem. A*, 2017, **5**, 17221-17229.
6. J. Shan, C. Guo, Y. Zhu, S. Chen, L. Song, M. Jaroniec, Y. Zheng and S.-Z. Qiao, *Chem*, 2019, **5**, 445-459.
7. L. Cao, Q. Luo, J. Chen, L. Wang, Y. Lin, H. Wang, X. Liu, X. Shen, W. Zhang, W. Liu, Z. Qi, Z. Jiang, J. Yang and T. Yao, *Nat Commun*, 2019, **10**, 4849.
8. H. Su, X. Zhao, W. Cheng, H. Zhang, Y. Li, W. Zhou, M. Liu and Q. Liu, *ACS Energy Lett.*, 2019, **4**, 1816-1822.
9. J. Yin, J. Jin, M. Lu, B. Huang, H. Zhang, Y. Peng, P. Xi and C. H. Yan, *J. Am. Chem. Soc.*, 2020, **142**, 18378-18386.
10. H. Guo, Z. Fang, H. Li, D. Fernandez, G. Henkelman, S. M. Humphrey and G. Yu, *ACS Nano*, 2019, **13**, 13225-13234.
11. S. Laha, Y. Lee, F. Podjaski, D. Weber, V. Duppel, L. M. Schoop, F. Pielhofer, C. Scheurer, K. Müller, U. Starke, K. Reuter and B. V. Lotsch, *Adv. Energy Mater.*, 2019, **9**, 1803795.
12. Z. Zhuang, Y. Wang, C. Q. Xu, S. Liu, C. Chen, Q. Peng, Z. Zhuang, H. Xiao, Y. Pan, S. Lu, R. Yu, W. C. Cheong, X. Cao, K. Wu, K. Sun, Y. Wang, D. Wang, J. Li and Y. Li, *Nat Commun*, 2019, **10**, 4875.
13. D. Liu, Q. Lv, S. Lu, J. Fang, Y. Zhang, X. Wang, Y. Xue, W. Zhu and Z. Zhuang, *Nano Lett.*, 2021, **21**, 2809-2816.
14. Y. Li, W. Zhou, X. Zhao, W. Cheng, H. Su, H. Zhang, M. Liu and Q. Liu, *ACS Appl. Energy Mater.*, 2019, **2**, 7483-7489.
15. A. Oh, H. Y. Kim, H. Baik, B. Kim, N. K. Chaudhari, S. H. Joo and K. Lee, *Adv. Mater.*, 2019, **31**, 1805546.
16. Q. Feng, Q. Wang, Z. Zhang, Y. Xiong, H. Li, Y. Yao, X.-Z. Yuan, M. C. Williams, M. Gu, H. Chen, H. Li and H. Wang, *Appl. Catal. B*, 2019, **244**, 494-501.
17. M. Etzi Coller Pascuzzi, A. Goryachev, J. P. Hofmann and E. J. M. Hensen, *Appl. Catal. B*, 2020, **261**, 118225.

18. Y. Gu, Y. Min, L. Li, Y. Lian, H. Sun, D. Wang, M. H. Rummeli, J. Guo, J. Zhong, L. Xu, Y. Peng and Z. Deng, *Chem. Mater.*, 2021, **33**, 4135-4145.
19. M. Aizaz Ud Din, S. Irfan, S. U. Dar and S. Rizwan, *Chemistry*, 2020, **26**, 5662-5666.
20. Y. Lin, Z. Tian, L. Zhang, J. Ma, Z. Jiang, B. J. Deibert, R. Ge and L. Chen, *Nat. Comm.*, 2019, **10**, 162.